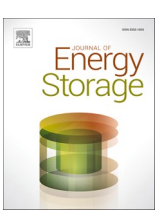
ELSEVIER

Contents lists available at ScienceDirect

Journal of Energy Storage

journal homepage: www.elsevier.com/locate/est



Research papers

Impact of cycling on the performance of mm-sized salt hydrate particles

Joey Aarts a,b, Hartmut Fischer, Olaf Adan, Henk Huinink a,b,*

- ^a Eindhoven Institute of Renewable Energy Systems, Eindhoven University of Technology, PO Box 513, Eindhoven 5600 MB, the Netherlands
- b Transport in Permeable Media Group, Department of Applied Physics, Eindhoven University of Technology, PO Box 513, Eindhoven 5600 MB, the Netherlands
- ^c TNO Materials Solution, High Tech Campus 25, Eindhoven, the Netherlands

ARTICLE INFO

Keywords: Salt hydrates Thermochemical materials Heat storage Cyclic behavior Particles K₂CO₃

ABSTRACT

Potassium carbonate is shown to be a promising salt for thermochemical heat storage. For a thermochemical reactor application, the salt hydrate is manufactured in mm-sized particles. It is known that salt hydrate particles undergo swelling and cracking during cyclic testing. Therefore, in this work the influence of cycling on structural and morphological evolution is investigated and the resulting impact on the hydration performance. It is found that the incremental volume increase during cycling is independent of the density at which a particle is produced. With lower starting relative density particles are found to be stable for more cycles compared to particles produced with high starting relative densities. Powder formation at the particle surface starts as soon as the particle density is close to values reported for percolation thresholds. The morphological changes during cycling result in formation of isolated pores and a highly tortuous pore system. As a result, the effective diffusion coefficient for cycled particles is lower compared to what is predicted for as produced particles with similar porosity resulting in lower power output than expected based on porosity. The results from this work help in understanding the reasons for swelling, cracking, powder formation and decreased performance with cycling, laying the foundation for mitigating these unwanted effects.

1. Introduction

In the period 2000 till 2018 an average energy of about 300 PJ of energy is used for residential space heating in the Netherlands only [1]. Even though this energy is largely generated from fossil fuels, over the last years energy generation using photovoltaic (PV) and wind energy have been increasing exponentially [1]. To stay within the temperature limits agreed on in the Paris agreement, the contribution of renewable energy will increase even further [2].

A major downside to PV and wind energy is that they are an intermittent, location, and time dependent source of energy [3]. Therefore, storage is required for the surplus of energy generated during peak production and release during peak consumption. An example is solar energy, which is abundant in summer and must be stored until winter for heating purposes. Energy storage using salt hydrates is a viable option to store energy during peak supply and release this energy during peak demand due to its high energy density and loss free storage [4].

Salt hydrates release energy in the form of heat during hydration by means of incorporation of water molecules inside their crystal lattice. The reverse process (dehydration) occurs when heat is supplied, and the water molecules are removed from the crystal lattice.

A promising salt hydrate identified for seasonal heat storage is potassium carbonate (K_2CO_3) considering energy density, user conditions, costs and safety [5]. The reversible hydration reaction is given by

$$K_2CO_3(s) + 1.5 H_2O(g) \rightleftharpoons K_2CO_3 \cdot 1.5 H_2O(s).$$
 (1)

For useful application of salt hydrates in a thermochemical reactor bed, salt hydrate powder cannot be used. Reactor beds of powder result in a too high pressure drop, decreasing the reactor performance [6]. Therefore, the salt hydrate must be manufactured into larger mm-sized particles.

Several studies on the kinetic behavior of potassium carbonate exist. Kinetics on powder level has been investigated by Fisher et al. (2021) [7] and Gaeini et al. (2019) [8]. The exact mechanism of hydration as a two-step process and the existence of a metastable zone have been elucidated by Sögütoglu et al. (2019) [9]. A detailed study of the hydration kinetics of mm-sized particles was presented by Aarts et al. (2022) [10].

E-mail addresses: j.aarts@tue.nl (J. Aarts), hartmut.fischer@tno.nl (H. Fischer), olaf.adan@tno.nl (O. Adan), h.p.huinink@tue.nl (H. Huinink).

^{*} Corresponding author at: Eindhoven Institute of Renewable Energy Systems, Eindhoven University of Technology, PO Box 513, Eindhoven 5600 MB, the Netherlands.

Cyclic experiments on powder performed by Sögütoglu et al. (2018) showed that potassium carbonate powder is cyclically stable with respect to hydration enthalpy [11]. When larger (irregular) grains were used, Beving et al. (2020) showed that these grains suffered from swelling and cracking over multiple cycles [12].

Due to the promising nature of K_2CO_3 as thermochemical material different composites containing K_2CO_3 have been manufactured to stabilize the material. The most used host matrix found for K_2CO_3 is vermiculite. By impregnating K_2CO_3 into vermiculite the commonly observed stability issues could be mitigated. Due to the porous nature of the host matrix enhanced reaction kinetics were observed and it was possible to use the deliquescence transition [13,14]. The fast vapor diffusion in the host matrix results in the overall hydration becoming nucleation limited (at 25 °C) and phase-boundary control (at 40 °C), in contrast to diffusion limited for pure salt particles [7]. Impregnation of K_2CO_3 into expanded graphite resulted in an increase in thermal conductivity in addition to the increased kinetics [15].

Recently modeling approached for K_2CO_3 packed bed have been developed to study the heat and mass transfer in packed bed reactor configurations. Mahmoudi et al. (2021) shows how heat transfer from neighboring particles may affect the hydration kinetics of a single particle [16]. The effect of a honeycomb heat exchanger on reactor bed performance is investigated by Kant et al. (2021) and the effect of bed diffusive properties on bed performance is investigated by Mikos-Nuszkiewicz et al. (2023) [17,18].

Although numerous literature research on K_2CO_3 has been performed, a detailed cyclic study of well-defined mm-sized particles has not yet been performed, even though understanding the effect of cycling on particle integrity and performance is important for long term application.

Therefore, in this work well defined mm-sized K_2CO_3 particles, as studied in previous work to elucidate the hydration mechanism [10], are subjected to cyclic hydration/dehydration tests to examine the effect of cycling on the geometry, morphology and kinetic performance. The approach from this work is aimed at providing a deeper understanding of the changes that occur with cycling and the impact of these changes. The results provide new insights into possibilities for material manipulation, keeping in mind the targeted application.

2. Materials and methods

2.1. Particle manufacturing and cyclic tests

Potassium carbonate sesquihydrate (provided by Evonik Functional Solutions GmbH) has been milled using a Fritsch planetary ball mill and sieved into a 300–500 $\mu \rm m$ fraction. Pressing of cylindrical particles was performed using a PO-Weber PW-40 2 column press (pressure range of 1–9 kbar). This resulted in cylindrical particles with a radius of 6.1 mm and variable heights (~2.2 mm) and densities (86–96 %). Lower pressures (<1 kbar) result in mechanically unstable particles and are therefore not used. It was confirmed no water was pressed out of the particle during pressing by comparing the powder weight to the particle weight.

The density of particles was determined by dividing the weight of the particle by its volume measured with a Mitutoyo digital caliper. The relative densities were calculated by dividing the measured density $\rho_{\rm g}$ [g·cm $^{-3}$] by the theoretical crystal density $\rho_{\rm c}$ [g·cm $^{-3}$] (2.18 g·cm $^{-3}$ for hydrated and 2.43 g·cm $^{-3}$ for anhydrous material) [19,20]. The total porosity $\varepsilon_{\rm t}$ [–] is defined as

$$\rho_{rel} = \frac{\rho_{\rm g}}{\rho_{\rm c}} = 1 - \varepsilon_{\rm t}.\tag{2}$$

The absolute error in density measurements is estimated to be 0.01 (1 % when the density is expressed in percentages).

Dehydration was performed overnight at 130 °C in an oven. Full

dehydration was confirmed by measuring the weight loss. Hydration was performed at 20 $^{\circ}$ C and 33 $^{\circ}$ C relative humidity (RH, saturated MgCl₂ solution [21]) inside a desiccator until full conversion was reached. Full conversion was determined by comparing the final uptake with the theoretical value based on the anhydrous mass. The anhydrous particles were placed inside the desiccator with one side (bottom) shielded from water vapor to ensure 1D water vapor diffusion. The particle weight was recorded by briefly taking it from the desiccator, weighing it and putting it back with the same side down as before. The measurement conditions were chosen such that deliquescence conditions and nucleation problems due to metastability are avoided [9]. To ensure a homogenous distribution of water vapor a small ventilator was placed inside the desiccator. Using this set-up with static RH conditions, possible fluctuations in measurement conditions were prevented as much as possible.

Fig. 1A shows the schematic set-up of the desiccator in which the particle (orange) is placed above a saturated $MgCl_2$ solution together with a fan for effective distribution of the humidity (33 % RH). Fig. 1B shows the general procedure from the starting material to the cyclic testing as described in this section.

2.2. Morphology analysis using Scanning Electron Microscopy (SEM)

SEM analysis was performed on a FEI Quanta 600 using high vacuum ($<10^{-4}$ mbar) and 10–20kV beam voltage. When analyzing mm-sized particles, prior to analysis the particles were cryogenically (liquid N_2) fractured to be able to analyze the particle cross section.

2.3. Compressive behavior

Compressive tests are performed at a compressive strain rate of 0.5 $\rm mm\cdot s^{-1}$ on a TestWinner 922. For measurements the cylindrical particle is placed on its curved side (Fig. 2). Compression in this direction is believed to be the most realistic compressive direction in a device application. In a real application curved instead of flat particles will be used

2.4. Skeletal density pycnometer measurements

The skeletal density and inaccessible porosity were measured on a Micromeritics AccuPyc II 1340 with Helium, Nitrogen and Argon gas all of grade 5 purity. The sample chamber was flushed 5 times using the specified analysis gas prior to the actual measurements. The sample density was measured 10 times of which the average and standard deviation were computed.

2.5. Effective diffusion coefficients using wet cup experiments

Wet cup experiments were performed according to the following procedure. A vial was filled partially with a saturated solution of LiCl. A surplus of LiCl powder was added to ensure a continuous saturated solution and constant RH (11 % [21]) throughout the complete experiments. A completely hydrated particle was placed on the inside of a screw cap which had a hole drilled in the top. Against the bottom of the particle a rubber ring was placed with an outer diameter equal to the inside of the screw cap and an inner diameter equal to the diameter of the hole in the top of the screw cap. The screw cap (containing the particle and rubber ring) was then screwed onto the vial containing the saturated LiCl solution so that the rubber ring pressed the particle firmly against the top of the screw cap. The connection was then wrapped in parafilm after which the vial was placed in a desiccator with saturated MgCl₂ solution (33 % RH [21]) (Fig. 3).

After specific time intervals the weight was recorded, and a permeability was calculated as follows [22]

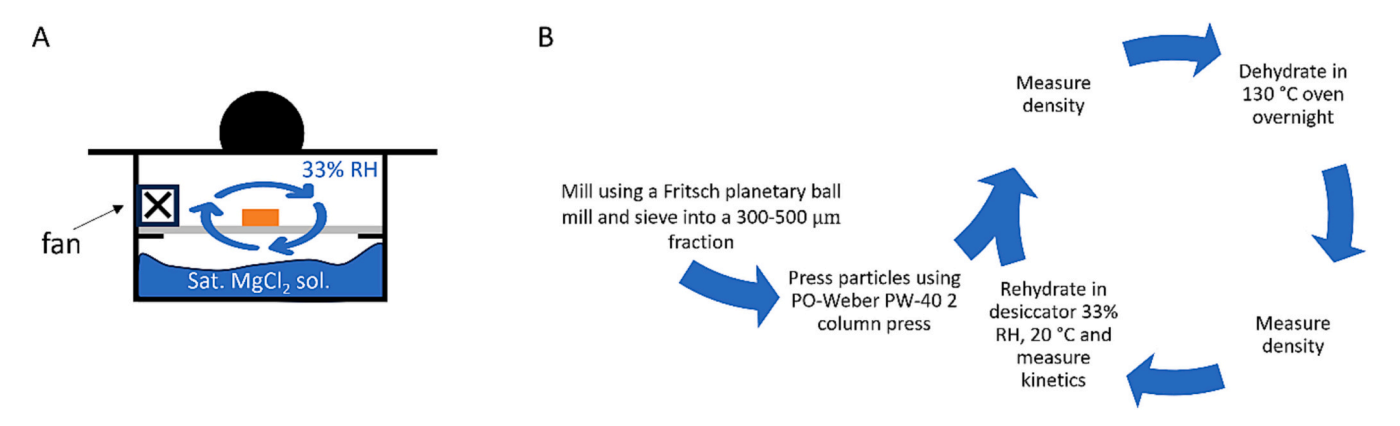


Fig. 1. Schematic set-up of the desiccator in which the particle (orange) is placed above a saturated $MgCl_2$ solution (33 % RH) together with a fan (A). Flow chart of the procedure taken from the fresh powder to the cyclic tests (B).

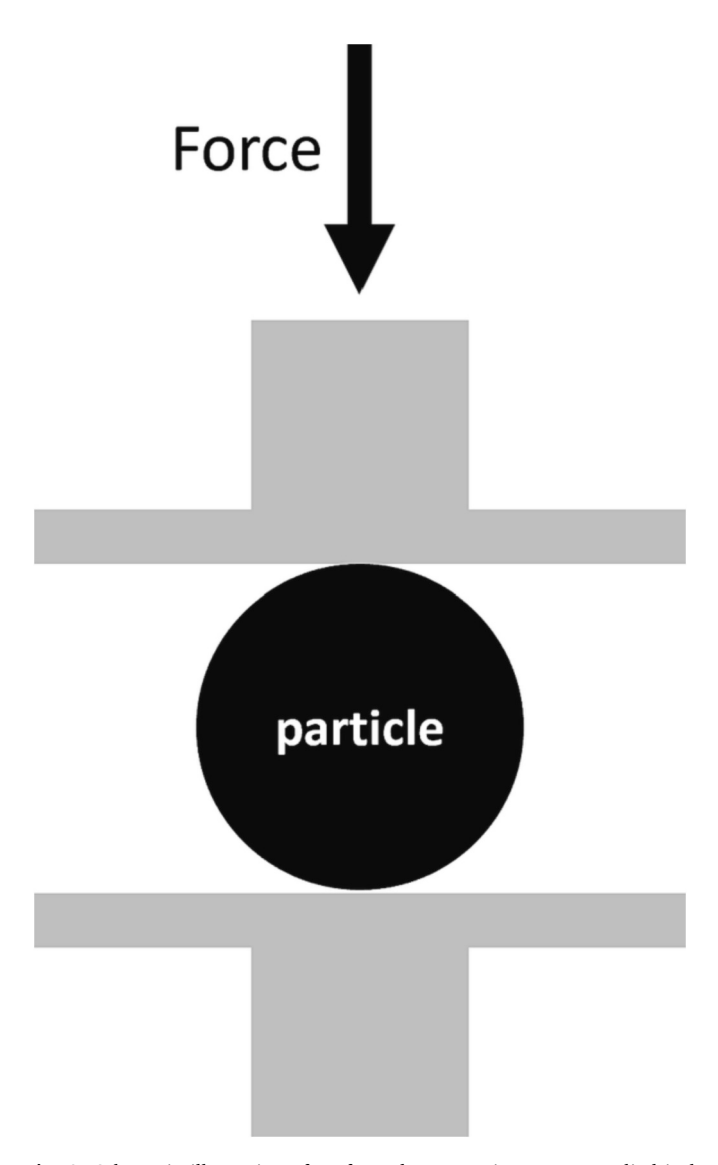


Fig. 2. Schematic illustration of performed compression tests on cylindrical mm sized $\rm K_2CO_3$ particles.

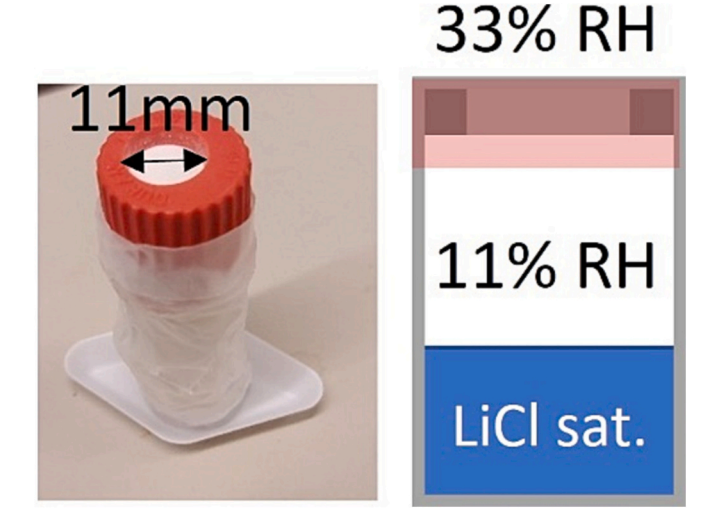


Fig. 3. Picture and schematic illustration of the used wet cup system.

$$P = \frac{\Delta m}{\Delta t} \frac{l}{A \Delta p}.$$
 (3)

Here $P\left[\mathrm{g.Pa^{-1}\cdot s^{-1}\cdot m^{-1}}\right]$, $l\left[\mathrm{m}\right]$, $A\left[\mathrm{m}^2\right]$ and $\Delta p\left[\mathrm{Pa}\right]$ are the permeability, thickness, surface area, and pressure difference, respectively. Lastly, $\Delta m\left[\mathrm{g}\right]$ and $\Delta t\left[\mathrm{s}\right]$ represent the mass and time difference, respectively.

Using Fick's law the permeability was then converted into an effective diffusion coefficient as follows

$$D_{\rm eff} = \frac{P \cdot R \cdot T}{M}.\tag{4}$$

Here $D_{\rm eff}$ [m²·s⁻¹] represents the effective diffusion coefficient, M [g·mol⁻¹] the molar mass of water, R [J·mol⁻¹·K⁻¹] the universal gas constant and T [K] the temperature.

2.6. Macro pore analysis using Mercury Intrusion Porosimetry (MIP)

MIP was conducted on a Micromeritics AutoPore IV 9500 using a mercury pressure range from 7 * $10^{-4}\pm0.1$ % MPa to 228 \pm 0.1 % MPa. Hydrated particles were measured as they were pressed or hydrated without further treatment.

3. Results and discussion

3.1. Structural evolution during cycling

First the external structural evolution is examined using mm-sized particles made with different initial densities (porosities). The volume increase ΔV [%] is measured relative to the starting material as produced (hydrate at cycle number 0) as follows

$$\Delta V = \frac{V_{\rm i}}{V_0} \cdot 100\%. \tag{5}$$

Here V_i [m³] and V_0 [m³] represent the cycled and initial particle volume, respectively. In Fig. 4 the volume increase over cycling for the hydrous and anhydrous state of the particle is given for various initial densities. A single cycle (cycle number) is considered as full dehydration followed by full hydration.

The volume increase of the salt hydrate particles is independent of their initial density and can be approximated with a linear fit for both the hydrous and anhydrous material (dashed lines in Fig. 4). Comparing the slopes of both linear lines, a slope of 15.5 \pm 0.5 % and 14 \pm 1 % is found for the hydrous and anhydrous material, respectively. Since the 86 % initial density particle started to lose powder after 6 cycles, only the volume increase for the first 6 cycles is given in Fig. 4.

The fact that the volume increase in hydrated and dehydrated state are independent of the starting density (porosity) suggests that the volumetric changes originate from something which is similar in all samples, and not the macroscopic porosity. Therefore, the nature of the particle swelling must be searched for in the individual grains within the particles.

Because of particle swelling, degradation occurs after several cycles. The particle appearance and degradation varies for different initial (hydrate) densities (Fig. 5).

The maximum number of cycles the TCM particle can sustain decreases with increasing initial (hydrate) density. Whereas the particle with 96 % density already fractures after 4 cycles, the particle produced with 86 % density fractures after 12 cycles.

This is underlined by comparing compression tests of uncycled particles with different densities (Fig. 6). Here the strain ω [%] is calculated by dividing the displacement d [mm] by the initial particle diameter d_0 [mm] and multiplying with 100 %.

The particles with the lowest hydrate density (88 %) show continuous cracking with increasing strain. Some of these small cracks are

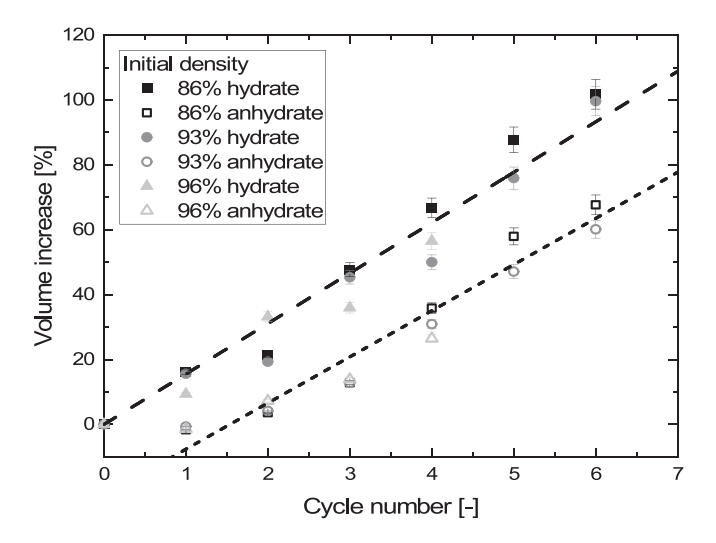


Fig. 4. Volume increase relative to the starting material (as produced in hydrated state; hydrate at cycle 0). The dashed lines represent a linear fit through the hydrous and anhydrous data. Hydrous and anhydrous datapoints are displayed as closed and open symbols, respectively.

visible during compaction. For the intermediate density (94 %) initially a steep increase in force is observed, followed by a steep decrease in force. Parts of the particle broke off from the parent particle, after which the remaining particle completely cracked at around 10 % compressive strain. The particles with the highest density (97 %) showed the steepest increase in force, after which they violently cracked from top till bottom and broke into multiple smaller chunks. Similar results are found in literature for porous ceramics with varying porosities [23].

The findings from Fig. 6 support the observations in Fig. 5. A lower density particle is better at accommodating cracks formed, independent of the crack origin, due to the internal porosity. This porosity results in crack tip blunting when a crack encounters a pore, decreasing the length of the formed crack and increasing the fracture toughness [24]. With increasing density (lower porosity), therefore a lower fracture toughness is observed, and crack propagation is easier once the required stress is achieved. As a result, due volume changes during cyclic dehydration/hydration, a lower density particle shows continuous cracking before complete fracturing at higher cycle number, and a higher density particle will show instantaneous cracking at a lower cycle number.

Another observation made in Fig. 5 is the formation of a cauliflower type of structure on the surface of the particle (see Fig. 7). During further cycling the particle rapidly loses powder from its surface possibly due to this cauliflower structure.

The loss of powder can also be seen in Fig. 8 where after cycle 6 for the lower density particle (86 %) a decrease in particle mass is observed due to the loss of powder. The other two particles with higher densities show a constant mass over cycling.

After cycle 6 it was still possible to measure the relative density of the particle with an initial hydrate density of 86 % by using the new mass (decreased due to powder loss) and slowly decreasing volume (due to powder loss). After 6 cycles the relative density of the hydrous material stabilizes around a density of 35–38 % (Fig. 8). The same holds for the anhydrous density which stabilizes around a density of 30–33 %. These densities are equal to the volume fraction of salt within the total particle (salt volume and pore volume).

Since stabilization of the relative density is occurring, the loss of powder is countered by a decrease in volume which indicates a threshold density (salt volume fraction) for particle stability exists. This threshold could be explained using percolation theory. In percolation theory the percolation threshold (threshold of volume occupied by particles) is the volume fraction of particles required to make long range connected structures (clusters). Passing the percolation threshold is general associated with drastic changes in materials properties, and is sometimes defined as a kind of phase transition [25]. An example often found in literature is related to conductivity which drastically increases above the percolation threshold of a certain additive [26,27].

The percolation thresholds for various 3D geometries, which can be used to approximate the grain geometry inside a salt particle, are given in Table 1. The percolation thresholds for these geometries are just below the relative density of the hydrous (35–38 %) and anhydrous (30–33 %) material. Therefore, the loss of powder from the larger particles is most probably associated with passing the percolation threshold, losing long range structural connectivity. Due to the loss of powder, the relative density of the remaining structure remains constant and above the percolation threshold.

3.2. Internal morphological changes during cycling

To shed further light on the powder formation during cycling the internal structure of the particles was investigated. SEM images on cross sections of hydrated material as produced, after 1 cycle and after 5 cycles were taken and are given in Fig. 9. For all three samples a porous structure is observed which is retained over cycling. However, on the grain level morphological changes occur. The grains in the particle as produced have a smooth surface whereas the grains after 1 hydration consist of multiple smaller grains. After 5 hydrations the picture has not

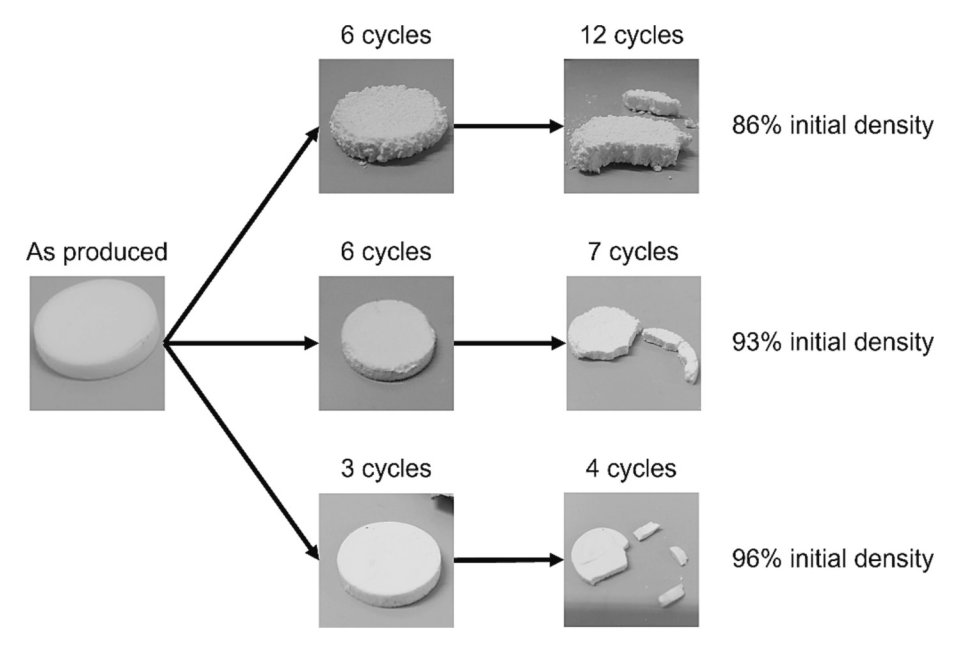


Fig. 5. Visual inspection of cycled tablets made with various initial (hydrate) densities. No visual cracks were observed before complete fracturing to the particle.

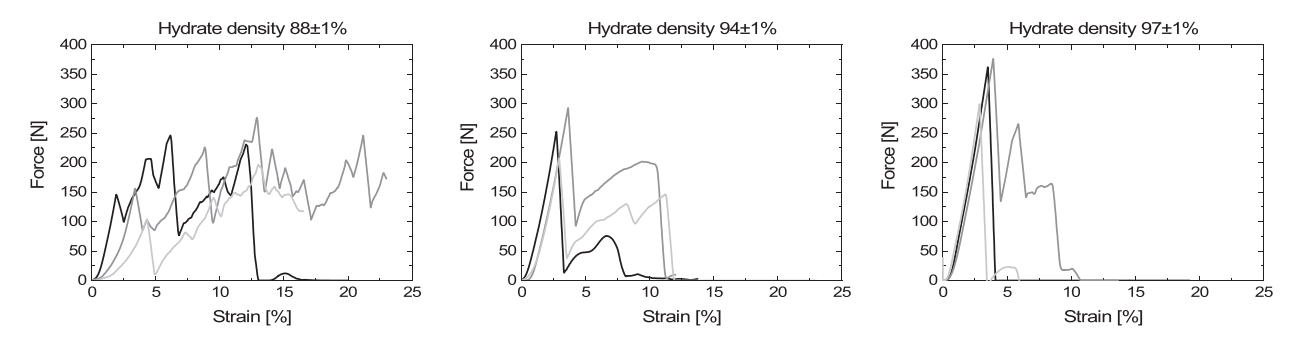


Fig. 6. Force versus compressive strain for particles with varying hydrate densities. The average height of all particles was equal to 6.8 ± 0.3 mm. For compression the particles were placed on their curved side while using a compression rate of 0.50 mm/min. For each density three samples were tested for reproducibility.

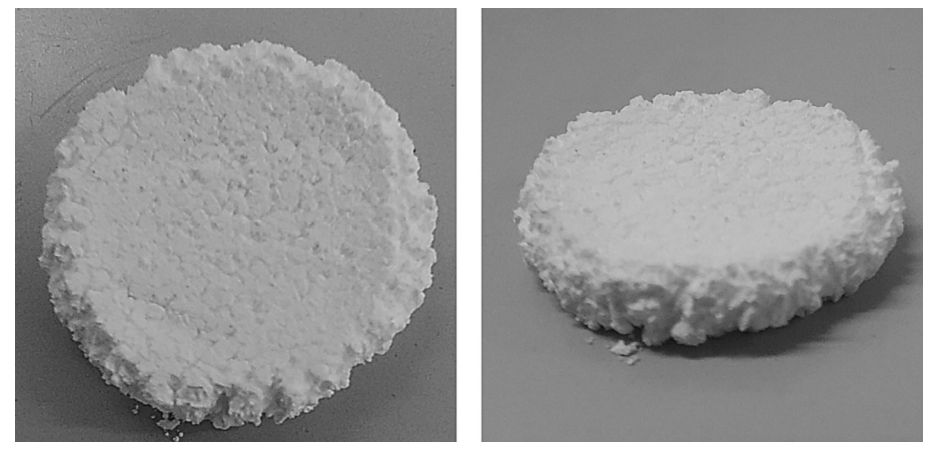


Fig. 7. Close up for a particle with an initial density of 86 % after 6 cycles.

changed compared to a single hydration. Images giving similar results obtained from the particle surface can be found in Supplementary information SI 1.

When using a larger magnification, the grains forming the parent grains are found to have sub-micron size (Fig. 10). After 5 hydrations these sub-micron grains seem to have decreased in size. The formation of

these grains might be the basis for the powder loss at the surface during cycling at higher cycle numbers, due to crossing of the percolation threshold.

The fact that the sub-micron grains are all similar in size suggests that nucleation of the hydrate phase occurs homogenously throughout the formed wetting layer during hydration. The wetting layer is a liquid

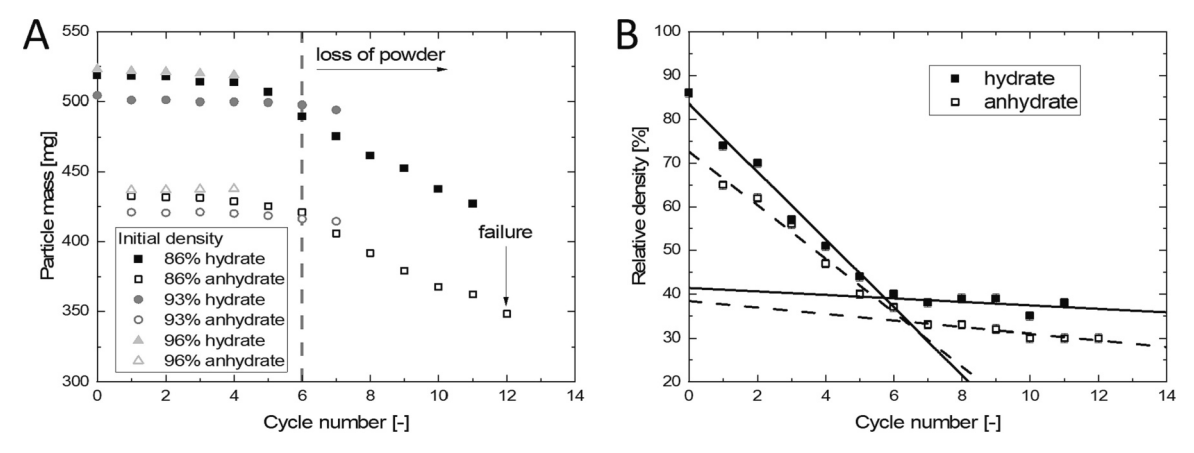


Fig. 8. Hydrous (closed symbols) and anhydrous (open symbols) sample mass at full hydration and dehydration for various cycles (A). The grey dashed line represents cycle number 6. Relative density of the hydrous and anhydrous particle (with initial density of 86%) over cycling (B). The solid black lines represent a linear fit through cycle number 0 till 6 and 7 till 11 for the hydrated material. The dashed black lines represent a linear fit through cycle number 1 till 6 and 7 till 12 for the anhydrous material.

Table 1Site percolation threshold values for various 3D geometries [28].

Geometry	Site percolation threshold [-]	
Sphere	0.3418	
Cube	0.2443-0.2485	
Cylinder $h = 2a$	0.4669	
Spherocylinder $h = 2a$	0.2972	
Icosahedron	0.3030	
Decahedron	0.2949	
Oblate spheroid $a = c = 2b$	0.3022-0.3050	
Prolate spheroid $a = c = b/2$	0.3022-0.3035	

boundary layer containing water and dissolved ions which forms on the surface of the anhydrous material during hydration. Since hydration proceeds outside of the metastable zone, nucleation is also instantaneously after which the nuclei grow equally in all directions [9,29]. The exact shape and size are then determined by the precise supersaturation conditions [30].

To better characterize the pore structure nitrogen sorption and mercury intrusion were performed. Nitrogen sorption showed the absence of micro and mesopores and further analysis was therefore abandoned. Mercury intrusion was conducted to investigate the macro pore evolution after hydration (Fig. 11). It is observed that the cumulative pore volume has increased after a single hydration which matches with the observation of a porosity increase. When comparing the pore size distribution, it is observed that broadening of the distribution occurs with an emphasis towards smaller pore diameters. Therefore, it can be concluded that the macropore structure changes towards the formation of smaller pore diameters, as also observed with SEM, while the grains themselves change into sub micrometer structures.

3.3. Impact of cycling on effective diffusion coefficients

Finally, the effect of cycling and the associated particle geometry and morphology changes on the reaction kinetics is investigated. Three particles with different initial densities were cyclically tested. Hydration was performed in a desiccator at 20 $^{\circ}$ C and 33 $^{\circ}$ RH until full conversion. Dehydration occurred overnight in an oven at 130 $^{\circ}$ C. The penetration depths of the 1D hydration front according to Aarts et al. (2022) [10] over various cycles are given in Fig. 12.

Fitting of the penetration depths in Fig. 12, to find the effective diffusion coefficients $D_{\rm eff}$ [mm²·s⁻¹], was done in the same manner as described in previous work [10]. The results are plotted in Fig. 13 with the respective hydrate particle density (porosity) at the x-axis.

In Fig. 13 the effective diffusion coefficient of the first hydration matches with the measured values from Aarts et al. (2022) for noncycled particles [10]. However, with cycling the effective diffusion coefficient starts to deviate from the measured values of freshly prepared particles with the same porosity resulting in much lower values. Several reasons may cause this: a decrease in accessible porosity and an increase in tortuosity or an increase in surface adsorption.

First the possibility of isolated pore formation with cycling is investigated. Gas pycnometer experiments were performed using various gases with various kinetic diameters. The kinetic diameter of gas molecules is determined by molecular sieves experiments and determines the minimum pore diameter the molecule can enter [31].

Pycnometer experiments were performed using helium, argon, and nitrogen gas. Helium can be used to find pores isolated for water vapor, due to a similar kinetic diameter, whereas argon and nitrogen are used to find pores still accessible for water vapor but in which diffusion will be slow [32–37]. The relative skeletal density was calculated by dividing the measured skeletal density by the maximum skeletal density of 2.18 $g \cdot cm^{-3}$ for hydrated potassium carbonate [20].

The skeletal densities found are independent of the used gas, which indicates that the pores giving the lower relative densities are solely isolated pores. When using Helium gas, the non-cycled (as produced) sample resulted in a relative skeletal density of 100 %, whereas the samples after 1 and 5 hydrations have a relative skeletal density of 97 and 94 % respectively. Now the ratio of closed pore volume $V_{\rm c}$ [m³] over the total pore volume $V_{\rm p}$ [m³] can defined as

$$\frac{V_c}{V_p} = \frac{\varepsilon_s (1 - \varepsilon_t)}{(1 - \varepsilon_s)\varepsilon_t}.$$
 (6)

Here ε_s [–] and ε_t [–] equal the skeletal and total porosity, respectively. The results for the pycnometer measurements using Helium are summarized in Table 2.

The non-cycled (as produced) particles do not have any closed pores and the full pore space is accessible for water vapor, whereas the cycled samples contain a significant number of closed pores reducing the available pore space for water vapor transport. However, this relatively small fraction of inaccessible pores cannot be solely responsible for the large difference of the effective diffusion coefficients.

Next, the possibility of an increase in tortuosity resulting in lower diffusion coefficients is discussed. In the uncycled samples the grains are non-porous, and diffusion occurs only through the main pores. When the sample is subjected to a hydration cycle these large grains turn into an assembly of multiple smaller grains with sizes very small (1 μm) compared to the parent grain (100–200 μm , Figs. 9 and 10).

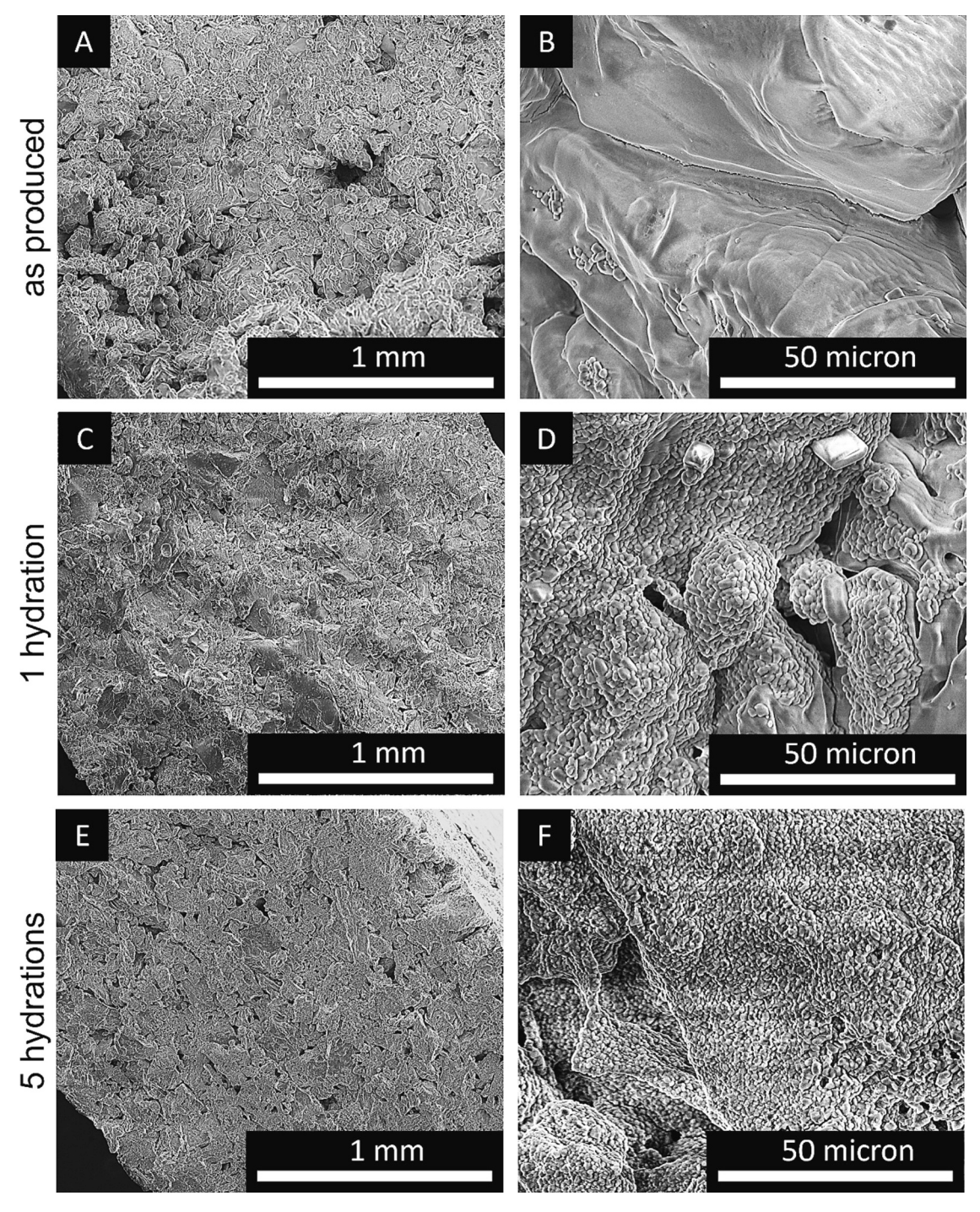


Fig. 9. Cross-section SEM images of hydrated K_2CO_3 particles made from a 300–500 μ m powder fraction with 78 \pm 1 % initial density as produced (A and B), after 1 hydration (C and D) and after 5 hydrations (E and F). The scale is indicated by the white bar.

Since the small grains are much smaller in diameter than the parent grain, the main pore can be considered as a straight pore with a tortuosity of 1 considering the length scale of a single small grain. As a result, the assembly of smaller grains is a more tortuous system in which the effective diffusion coefficient is expected to be significantly lower compared to the main pores (Fig. 14).

In addition, formation of blind pores can lower the effective diffusion coefficient by increasing the tortuosity of the system.

A final possible explanation is the adsorption and diffusion of water on the additional surface created during cyclic testing. For NaCl particles it is know that at vapor pressures far below the deliquescence water vapor pressure, adsorption of surface water occurs [38]. This surface

water can translate across the salt surface resulting in the transport of water molecules which possibly affects the overall effective diffusion coefficient [39]. Recent work by Houben et al. (2022) shows that similar adsorption of water on the hydrate surface occurs for K₂CO₃ [40].

To further illustrate the effect of morphological changes during cycling on $D_{\rm eff}$, wet-cup experiments using fully hydrated cylindrical particles were performed, in which only transport occurs in the absence of hydration. The results for the effective diffusion coefficients are given in Fig. 13. It is found that the effective diffusion coefficients for the noncycled (as produced) and cycled samples match with the observed trends for both materials. This results in two conclusions:

First, the studied systems are fully diffusion limited during hydration

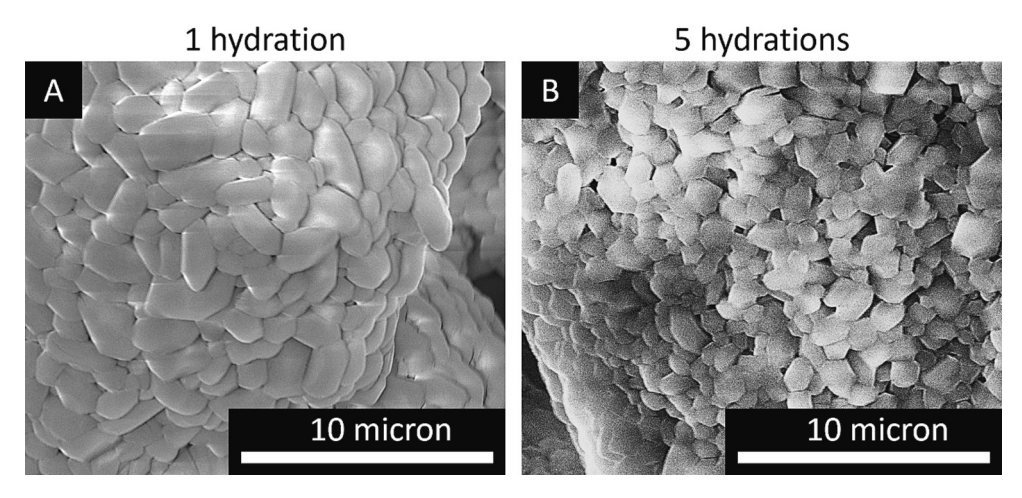


Fig. 10. Cross-section SEM images of hydrated K_2CO_3 particles made from a 300–500 μm powder fraction with 78 \pm 1 % initial density as produced (A) and after 5 hydrations (B). The scale is represented by the white bar.

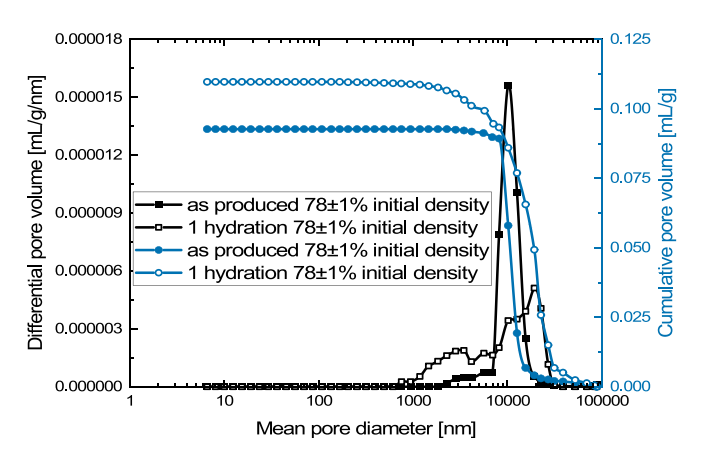


Fig. 11. MIP intrusion curves of a pristine particle with 78 ± 1 % initial density and a particle with initial density of 78 ± 1 % which underwent 1 hydration cycle.

experiments. If this would not be the case the effective diffusion coefficients from kinetic analysis (hydration experiments) and wet cup experiments would differ. Second, the difference in diffusion coefficients for uncycled and cycled samples only originates from morphological changes (and not chemical), since hydration is absent during wet cup experiments.

To investigate the effect of swelling and decreased water vapor diffusion on particle performance, the average power output per hydrous volume $P_{50\%}$ [W·m $^{-3}$] or kilogram of anhydrous material

$$P_{50\%}\left[\text{W}\cdot\text{kg}^{-1}\right]$$
 at 50 % conversion can be calculated as
$$P_{50\%} = \frac{N_{\text{water}}\cdot\Delta H}{N_{\text{water}}\cdot\Delta H},$$
 (7)

$$P_{50\%} = \frac{N_{\text{water}} \cdot \Delta H}{t_{50\%} \cdot m_a}.$$
 (8)

Here $N_{\rm water}$ [mol] represents the reacted number of moles of water at 50 % conversion, $t_{50\%}[\rm s]$ the time it takes to reach 50 % conversion, ΔH the reaction enthalpy and V [m³] and m_a [kg] the total hydrated volume and anhydrous mass of the particle at the specific cycle, respectively. The reaction enthalpy is obtained from literature to be $\Delta H^{\rm e}=63.6$ kJ·mol $^{-1}$ [41]. The calculated power output in W·m $^{-3}$ and W·kg $^{-1}$ is given in Fig. 15.

From the figure it is visible that the power output per volume for the $86\,\%$ density particles does not change with cycling and even decreases during cycle 2. For the $93\,\%$ particle cycle 2 and 3 are lower compared to cycle 1 and after cycle 3 an increase in power is observed. For the $96\,\%$ particle a continuous increase is observed.

The reason for the decrease in power output (per volume and mass) for the 86 % and 93 % sample in cycle 2 is that the effective diffusion coefficient has decreased. This increases the time to reach 50 % conversion. In the remaining cycles for the 86 % and 93 % particle the slow increase in diffusion coefficient does not outweigh the volume increase, resulting in minimal changes in power output per volume with cycling. After 4 cycles the power output of the 86 % density particle slightly decreases. For the 96 % particle a continuous increase is observed. Since the initial porosity and effective diffusion coefficient are so low, small internal cracks formed during cycling aid the water vapor diffusion and

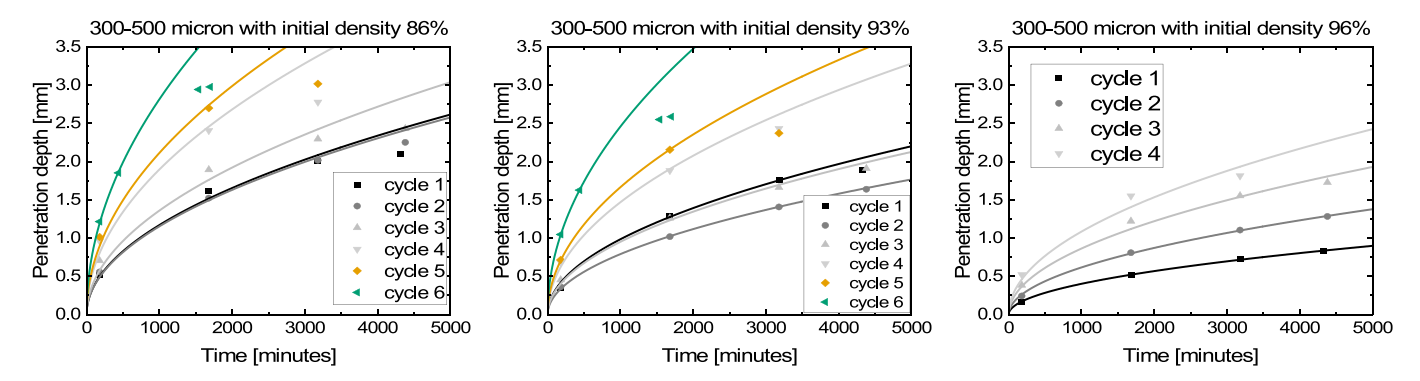


Fig. 12. Penetration depth versus time over cycling for various tablets with different initial densities. Fitting was performed as described in our previous work [10]. The data points represent measurement points whereas the solid lines correspond to the fits.

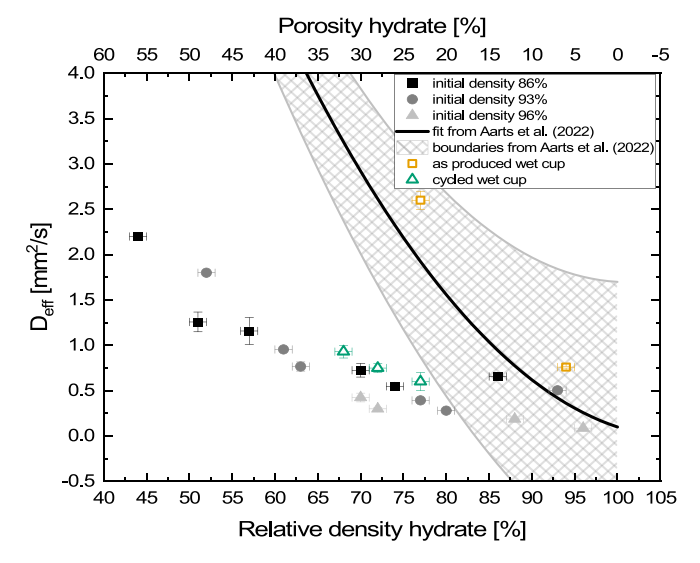


Fig. 13. Effective water vapor diffusion coefficients for various relative densities over cycling for particles with different initial densities (solid points). The effective diffusion coefficients were obtained from fitting Fig. 12. The solid black line represents the fit from Aarts et al. (2022), for non-cycled particles for which the measured values lay within the patterned area [10]. The open square and triangular symbols represent the effective water vapor diffusion coefficients from wet-cup experiments for as produced and cycled particles respectively.

are not canceled out by the increase in volume.

For the power output per kilogram the trend for the 93 % and 96 % particle is like that of the power output per volume. For the 86 % particle the power per kilogram is now continuously increasing after cycle 2. This indicates that in a reactor system, where the total reactor volume and mass remains constant, the overall particle power output increases with cycling for all three initial particle densities.

Cycling mm-sized particles leads to an increase in total porosity,

whereas some of this porosity is isolated and inaccessible for water vapor. Due to morphological changes the effective diffusion coefficient decreases compared to values known for uncycled particles. The fact that cycled samples perform worse as would be predicted from the as produced samples due to morphological changes opens pathways to find solutions to this problem.

4. Conclusion

Different well defined mm-sized K_2CO_3 particles with varying relative densities were subjected to cyclic hydration/dehydration cycles. The macroscopic and microscopic changes during different cycles have been assessed as well as the impact of these changes on the performance of the material.

The macroscopic volume increase of the particles was monitored with every cycle and found to be independent of the initial particle density. However, the cyclic lifetime was found to be influenced by the initial particle density. Particles with high relative densities were found to fracture at earlier cycles, whereas particles with lower relative densities lose powder upon cycling after which fracturing occurs. Compressive tests showed that particles with lower relative densities are better at accommodating crack formation, hence the longer cyclic lifetime.

The microscopic structure of the particle was studied using SEM which showed a morphological change occurring with cycling. It was observed that the internal morphology changes and the non-porous grains change into an assembly of micrometer sized smaller grains. With additional cycling the structure remains similar with a slight decrease in grain size.

Cycling hydration experiments showed that the effective diffusion coefficient for cycled particles was lower than that for non-cycled (as produced) particles with similar porosity. This results in a lower performance as is predicted for non-cycled (as produced) particles. Three possible reasons are given for the lower diffusion coefficients related to the observed morphological changes. First, isolated pores are formed.

 Table 2

 Geometrically determined relative particle density, pycnometer relative skeletal density and fraction of the total porosity closed to water vapor using Helium gas.

Particle state	Relative particle density [%]	Relative skeletal density [%]	Percentage of porosity closed [%]
As produced	77	99.9 ± 0.1	0
1 hydration	72	97.1 ± 0.5	8
5 hydrations	53	94.4 ± 0.8	7

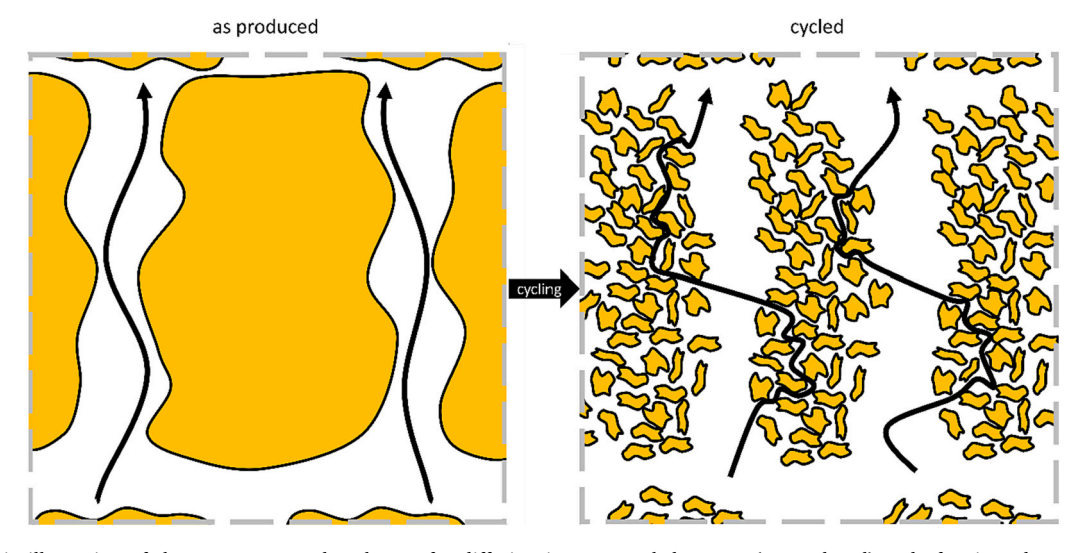


Fig. 14. Schematic illustration of the pore space and pathways for diffusion in an uncycled system (as produced) and after it underwent a full hydration cycle (cycled).

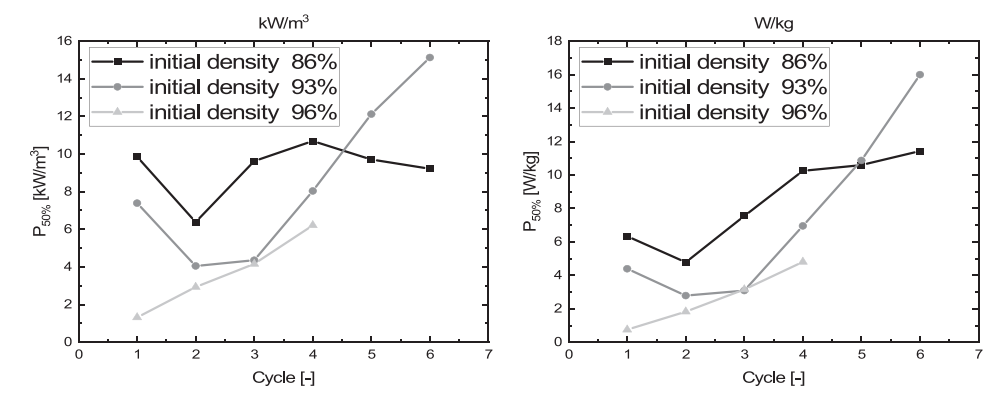


Fig. 15. Calculated average power output per hydrated volume and anhydrous mass at 50 % conversion for the particles in Fig. 12.

Second, an internal pore system with higher tortuosity than the noncycled (as produced) system is produced. Third, additional surface formation results in additional surface adsorption and surface transport. Future research must be conducted to examine to which extend each effect contributes.

Since the morphological changes affecting the particle performance and stability are most probably related to the crystallization behavior of the hydrate during hydration, the results from this work open new possible pathways to mitigate these effects. Such possibilities could be addition of additives to influence the crystallization behavior of the hydrate material during hydration. Furthermore, these results and methodology can be expanded to other salts as well to investigate the influence of cycling on the behavior of mm-sized particles made of different salts.

The presented work provides new insights into the volumetric and morphological changes occurring during cyclic testing of K_2CO_3 and the effects on the particle performance.

As a final remark it is important to note that particle behavior on a single particle level may vary from particle behavior inside a reactor bed. Additional effects like agglomeration could occur and the swelling behavior might change under confinement. Therefore, extensive cyclic studies on particle beds must be performed to accurately model and design a cyclically stable thermochemical reactor bed.

Supplementary data to this article can be found online at $\frac{https:}{doi.}$ org/10.1016/j.est.2023.109806.

CRediT authorship contribution statement

Joey Aarts: Conceptualization, Methodology, Writing – original draft, Visualization, Investigation. Hartmut Fischer: Conceptualization, Writing – review & editing. Olaf Adan: Conceptualization, Writing – review & editing, Supervision, Funding acquisition. Henk Huinink: Conceptualization, Writing – review & editing, Supervision, Funding acquisition.

Declaration of competing interest

The authors declare that they have no known competing financial interests or personal relationships that could have appeared to influence the work reported in this paper.

Data availability

Data will be made available on request.

Acknowledgements

The authors would like to thank Hans Dalderop for his technical support and Natalia Mazur for fruitful discussions. Jouk Hamelink from

Micromeritics Instrument Corporation and Lisette Wijkhuijs are gratefully acknowledged for helping with conducting gas pycnometer experiments. Evonik Functional Solutions GmbH is thanked for providing the potassium carbonate salt.

Funding

This project has received funding from the European Union's Horizon 2020 research and innovation programme under grant agreement No 869810. This work reflects only the author's view. The European Commission is not responsible for any use that may be made of this information.

References

- [1] The Netherlands-Countries & Regions IEA n.d. https://www.iea.org/countries/the-netherlands (accessed October 7, 2022).
- [2] The Paris Agreement, 2015.
- [3] X. Cao, X. Dai, J. Liu, Building energy-consumption status worldwide and the state-of-the-art technologies for zero-energy buildings during the past decade, Energ. Buildings 128 (2016) 198–213, https://doi.org/10.1016/j.enbuild.2016.06.089.
- [4] H. Jarimi, D. Aydin, Z. Yanan, G. Ozankaya, X. Chen, S. Riffat, Review on the recent progress of thermochemical materials and processes for solar thermal energy storage and industrial waste heat recovery, Int J Low-Carbon Technol 14 (2019) 44–69 https://doi.org/10.1093/iiitt/ctv052
- [5] P.A.J. Donkers, L.C. Sögütoglu, H.P. Huinink, H.R. Fischer, O.C.G. Adan, A review of salt hydrates for seasonal heat storage in domestic applications, Appl. Energy 199 (2017) 45–68, https://doi.org/10.1016/j.apenergy.2017.04.080.
- [6] Z.H. Pan, C.Y. Zhao, Gas-solid thermochemical heat storage reactors for hightemperature applications, Energy 130 (2017) 155–173, https://doi.org/10.1016/j. energy.2017. 04.102.
- [7] R. Fisher, Y. Ding, A. Sciacovelli, Hydration kinetics of K2CO3, MgCl2 and vermiculite-based composites in view of low-temperature thermochemical energy storage, J Energy Storage 38 (2021), 102561, https://doi.org/10.1016/j. est 2021 102561
- [8] M. Gaeini, S.A. Shaik, C.C.M. Rindt, Characterization of potassium carbonate salt hydrate for thermochemical energy storage in buildings, Energ. Buildings 196 (2019) 178–193, https://doi.org/10.1016/j.enbuild.2019.05.029.
- [9] L.-C. Sögütoglu, M. Steiger, J. Houben, D. Biemans, H.R. Fischer, P. Donkers, et al., Understanding the hydration process of salts: the impact of a nucleation barrier, Cryst. Growth Des. 19 (2019) 2279–2288, https://doi.org/10.1021/acs. crd 8b01908
- [10] J. Aarts, S. de Jong, M. Cotti, P. Donkers, H. Fischer, O. Adan, et al., Diffusion limited hydration kinetics of millimeter sized salt hydrate particles for thermochemical heat storage, J Energy Storage 47 (2022), 103554, https://doi. org/10.1016/j.est.2021.103554.
- [11] L.C. Sögütoglu, P.A.J. Donkers, H.R. Fischer, H.P. Huinink, O.C.G. Adan, In-depth investigation of thermochemical performance in a heat battery: cyclic analysis of K2CO3, MgCl2 and Na2S, Appl. Energy 215 (2018) 159–173, https://doi.org/ 10.1016/j.apenergy. 2018.01.083.
- [12] M.A.J.M. Beving, A.J.H. Frijns, C.C.M. Rindt, D.M.J. Smeulders, Effect of cycle-induced crack formation on the hydration behaviour of K2CO3 particles: experiments and modelling, Thermochim. Acta 692 (2020), 178752, https://doi.org/10.1016/j.tca.2020.178752.
- [13] A.I. Shkatulov, J. Houben, H. Fischer, H.P. Huinink, Stabilization of K2CO3 in vermiculite for thermochemical energy storage, Renew. Energy 150 (2020) 990–1000, https://doi.org/10.1016/j.renene.2019.11.119.
- 990–1000, https://doi.org/10.1016/j. renene.2019.11.119.
 D. Zou, X. Yue, T. He, J. Ding, D. Ba, Experimental research on the preparation of K2CO3/expanded vermiculite composite energy storage material, Materials (Basel) 15 (2022) 3702, https://doi.org/10.3390/ma15103702.

- [15] Q. Zhao, J. Lin, H. Huang, Z. Xie, Y. Xiao, Enhancement of heat and mass transfer of potassium carbonate-based thermochemical materials for thermal energy storage, J Energy Storage 50 (2022), 104259, https://doi.org/10.1016/j. est.2022.104259.
- [16] A. Mahmoudi, P.A.J. Donkers, K. Walayat, B. Peters, M. Shahi, A thorough investigation of thermochemical heat storage system from particle to bed scale, Chem. Eng. Sci. 246 (2021), 116877, https://doi.org/10.1016/j.ces.2021.116877.
- [17] K. Kant, A. Shukla, D.M.J. Smeulders, C.C.M. Rindt, Performance analysis of a K2CO3-based thermochemical energy storage system using a honeycomb structured heat exchanger, J Energy Storage 38 (2021), 102563, https://doi.org/ 10.1016/j.est.2021.102563.
- [18] N. Mikos-Nuszkiewicz, P. Furmański, P. Łapka, A mathematical model of charging and discharging processes in a thermochemical energy storage reactor using the hydrated potassium carbonate as a thermochemical material, Energy 263 (2023), 125642, https://doi.org/10.1016/j.energy.2022.125642.
- [19] Villars P, Cenzual K, editors. K2CO3 (K2[CO3] rt mon1) Crystal Structure: Datasheet From "PAULING FILE Multinaries Edition – 2012" in SpringerMaterials (https://materials.springer.com/isp/crystallographic/docs/sd_1215403) n.d.
- [20] Villars P, Cenzual K, editors. K2CO3-1.5H2O (K4[CO3]2[H2O]3) Crystal Structure: Datasheet From "PAULING FILE Multinaries Edition – 2012" in SpringerMaterials (https://materials.springer.com/isp/crystallographic/docs/sd_0377610) n.d.
- [21] L. Greenspan, Humidity fixed points of binary saturated aqueous solutions, J Res Natl Bur Stand Sect A Phys Chem 81A (1977) 89, https://doi.org/10.6028/ ires.081A.011.
- [22] F.A. Joy, A.G. Wilson, Standardization of the dish method for measuring water vapor transmission, in: Int Symp Humidity Moisture, Proc, 1963, pp. 259–270.
- [23] S. Meille, M. Lombardi, J. Chevalier, L. Montanaro, Mechanical properties of porous ceramics in compression: on the transition between elastic, brittle, and cellular behavior, J. Eur. Ceram. Soc. 32 (2012) 3959–3967, https://doi.org/ 10.1016/j.jeurceramsoc.2012. 05.006.
- [24] Z.-Y. Deng, J. She, Y. Inagaki, J.-F. Yang, T. Ohji, Y. Tanaka, Reinforcement by crack-tip blunting in porous ceramics, J. Eur. Ceram. Soc. 24 (2004) 2055–2059, https://doi.org/10.1016/S0955-2219(03)00365-0.
- [25] D. Stauffer, Scaling theory of percolation clusters, Phys. Rep. 54 (1979) 1–74, https://doi.org/10.1016/0370-1573(79)90060-7.
- [26] J.C. Grunlan, W.W. Gerberich, L.F. Francis, Lowering the percolation threshold of conductive composites using particulate polymer microstructure, J. Appl. Polym. Sci. 80 (2001) 692–705, https://doi.org/10.1002/1097-4628(20010425)80: 4<692::AID-APP1146> 3.0.CO;2-W.
- [27] Y.P. Mamunya, Y.V. Muzychenko, P. Pissis, E.V. Lebedev, M.I. Shut, Percolation phenomena in polymers containing dispersed iron, Polym. Eng. Sci. 42 (2002) 90–100, https://doi.org/10.1002/pen.10930.

- [28] S. Torquato, Y. Jiao, Effect of dimensionality on the percolation threshold of overlapping nonspherical hyperparticles, Phys. Rev. E 87 (2013), 022111, https:// doi.org/10.1103/PhysRevE.87. 022111.
- [29] L.-C. Sögütoglu, F. Birkelbach, A. Werner, H. Fischer, H. Huinink, O. Adan, Hydration of salts as a two-step process: water adsorption and hydrate formation, Thermochim Acta 695 (2021), 178819, https://doi.org/10.1016/j. tca.2020.178819.
- [30] H. Lin, Z. Lei, Z. Jiang, C. Hou, D. Liu, M. Xu, et al., Supersaturation-dependent surface structure evolution: from ionic, molecular to metallic micro/nanocrystals, J. Am. Chem. Soc. 135 (2013) 9311–9314, https://doi.org/10.1021/ja404371k.
- [31] S. Kunze, R. Groll, B. Besser, J. Thöming, Molecular diameters of rarefied gases, Sci. Rep. 12 (2022) 2057, https://doi.org/10.1038/s41598-022-05871-y.
- [32] J.S. D'Arrigo, Screening of membrane surface charges by divalent cations: an atomic representation, Am J Physiol Physiol 235 (1978) C109–C117, https://doi. org/10.1152/ajpcell.1978. 235.3.C109.
- [33] O. Edidiong, S. Habiba, E. Gobina, Gas transport and characterization of inorganic ceramic membrane for lactic acid esterification, Proceedings of the World Congress on Engineering and Computer Science 2 (2014) 590–594.
- [34] R.W. Baker, Membrane transport theory, in: Membr. Technol. Appl, John Wiley & Sons, Ltd, Chichester, UK, 2012, pp. 15–96, https://doi.org/10.1002/0701119350696.ch2
- [35] N.W. Ockwig, T.M. Nenoff, Membranes for hydrogen separation, Chem. Rev. 107 (2007) 4078–4110, https://doi.org/10.1021/cr0501792.
- [36] S.S. Batsanov, Van der Waals radii of elements, Inorg. Mater. 37 (2001) 871–885, https://doi.org/10.1023/A:1011625728803.
- [37] J. Vogt, S. Alvarez, van der Waals radii of noble gases, Inorg. Chem. 53 (2014) 9260–9266, https://doi.org/10.1021/ic501364h.
- [38] M.E. Wise, S.T. Martin, L.M. Russell, P.R. Buseck, Water uptake by NaCl particles prior to deliquescence and the phase rule, Aerosol Sci. Tech. 42 (2008) 281–294, https://doi.org/10.1080/02786820802047115.
- [39] P. Cabrera-Sanfelix, A. Arnau, G.R. Darling, D. Sanchez-Portal, Water adsorption and diffusion on NaCl(100), J. Phys. Chem. B 110 (2006) 24559–24564, https:// doi.org/10.1021/jp062462q.
- [40] J. Houben, D. Langelaan, L. Brinkman, H. Huinink, H.R. Fischer, O.C.G. Adan, Understanding the hydration process of salts: the relation between surface mobility and metastability, Cryst. Growth Des. 22 (2022) 4906–4916, https://doi.org/ 10.1021/acs.cgd.2c00416.
- [41] D.D. Wagman, W.H. Evans, V.B. Parker, R.H. Schumm, I. Halow, S.M. Bailey, et al., The NBS tables of chemical thermodynamic properties: selected values for inorganic and C1 and C2 organic substances in SI units, J. Phys. Chem. Ref. Data Monogr. (1982), https://doi.org/10.18434/M32124.